Baryon Stopping and Equation of State in Heavy Ion Collision

M.Sc. Thesis

By

Sunil Jakhar

DISCIPLINE OF PHYSICS

INDIAN INSTITUTE OF TECHNOLOGY INDORE

June, 2016

Baryon Stopping and Equation of State in Heavy Ion Collision

A THESIS

Submitted in partial fulfillment of the

requirements for the award of the degree

of

Master of Science

by

Sunil Jakhar

DISCIPLINE OF PHYSICS

INDIAN INSTITUTE OF TECHNOLOGY INDORE

June, 2016

Acknowledgements

I would like to thank my thesis advisor Dr. Raghunath Sahoo, Department of Physics, Indian Institute of Technology, Indore for giving me his invaluable time, guidance, co-operation and constant encouragement and providing all the necessary facilities throughout the course of my studies and preparation of the manuscript in the present form.

I would like to thank the expert who was there for my help and I have learned many things since I came in touch with Dr. Prakhar Garg. He provided me unfailing support and continuous encouragement throughout my years of study during thesis writing. Special thanks to Dr. Swatantra Tiwari and Dhananjaya Thakur for valuable guidance and support in thesis work.

I would also like to acknowledge Dr. Trambak Bhattacharya, Sushanta, Arvind, Dhananjaya and Pragati and Pooja Didi for their support and all of my M.Sc classmates of Department of Physics, Indian Institute of Technology Indore.

Finally, I would like to convey my heartfelt gratitude and sincere appreciation to Prakhar, Swatantra and Aditya Bhaiya for being there in any need.

(Sunil Jakhar)

Contents

List of Figures

List of Tables

Chapter 1

Introduction

The ultimate building blocks of the matter as well as their interaction mechanisms has been always a quest for knowledge for human beings. The fundamental particles quarks and leptons along with their anti-particles form the composite objects. The interactions among these fundamental particles are mediated by gauge-bosons e.g., photons (γ), gluons (g), $W^{\pm}$, Z^0, and gravitons (G). Quarks (anti-quarks) exist in six different flavors and similarly there are six different types of leptons (anti-leptons) as well : electron (positron), muon (anti-muon), tau (anti-tau) lepton, and the corresponding three neutrinos (anti-neutrinos). Each quark (anti-quark) can exist in three possible colours e.g. red (anti-red), blue (anti-blue) and green (anti-green). These colour charges generate strong interactions among the quarks (anti-quarks). Quarks and anti-quarks form two different type of colour neutral bound states named as baryons (three quark states) and mesons (quark-antiquark states). Gluons that mediate the strong interactions between quarks, are bi-coloured vector particles and exist in eight possible kinds. Further, gluons have zero rest mass and spin 1. The theory which deals with quarks and gluons and their associated dynamics is known as Quantum Chromodynamics (QCD). This is similar to the interactions between two electrically charged particles (i.e. electromagnetic interaction), which is governed by Quantum Electrodynamics (QED). However, QCD is a non-abelian gauge theory in contrast to QED, which is an abelian gauge theory. The non-abelian nature of the QCD arises since the gluons carry colour charges and hence are self-interacting, while photons are electrically neutral particles and hence do not possess self-interactions. Two basic properties of the theory of QCD are:

- Asymptotic freedom and
- Color confinement.

The strong interaction between quarks and gluons at large distances (gives confinement) and asymptotic freedom at short distance are the two remarkable features of QCD, discovered by Gross, Politzer and Wilczek in 1973 [1]. According to the behavior of short and large distance, the static QCD potential can suitably be described as:

$$V_s = -\frac{4}{3} \times \frac{\alpha_s}{r} + k \times r, \tag{1.1}$$

where the first term dominates at small distance, arising from a single-gluon exchange, similar to the Coulomb potential between two charges in QED, while the second term is presumably linked to the confinement of quarks and gluons inside hadrons and is called string tension form.

The re-normalized effective QCD coupling $\alpha_s(\mu) = g_s^2/4\pi$ depends on the re-normalization scale (running coupling), similar to that in QED. However, the QED running coupling increases with energy scale, while the gluon self-interactions lead to a completely different behavior in QCD.

The running coupling constant α_s in QCD (at one loop) can be expressed in terms of a squared four momentum transfer Q^2, the number of quark flavors N_f, and the typical QCD scale $\Lambda_{QCD} \approx 0.2$ GeV [2, 3]:

$$\alpha_s(Q^2) = \frac{g_s^2}{4\,\pi} = \frac{12\,\pi}{(33 - 2\,N_f)\,\ln(\frac{Q^2}{\Lambda_{QCD}^2})}. \tag{1.2}$$

The running of α_s is confirmed precisely by experimental results as shown in Fig. 1.1 [4]. From Eq. (1.2), it is clear that $\alpha_s \to \infty$ when $Q^2 = \Lambda_{QCD}^2$, and $\alpha_s \to 0$ when $Q^2 \to \infty$. Thus the QCD scale parameter determines the strength of the coupling constant.

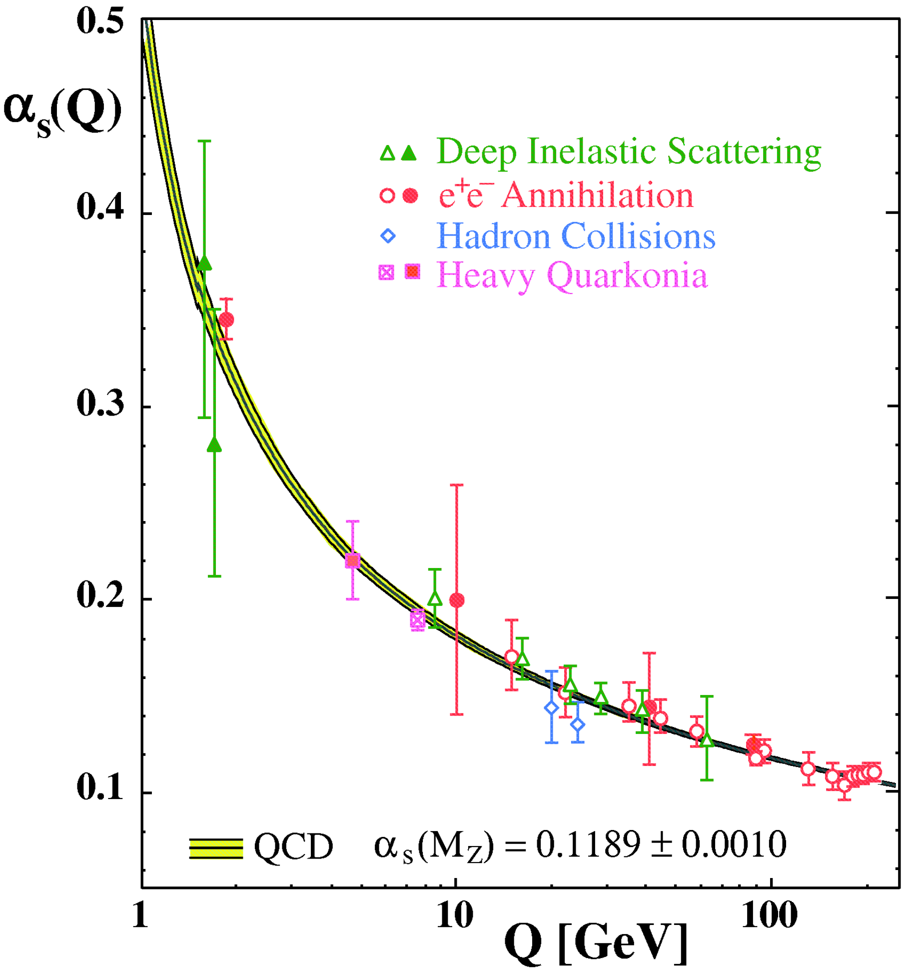

Figure 1.1: The running coupling constant, α_s as a function of energy scale Q, measured in different experiments and compared with theoretical calculations [5].

The infinite value of the running coupling constant when $Q^2 = \Lambda^2_{QCD}$ (i.e, the large distance limit) gives the "quark confinement" property of the QCD whereas zero value of the running coupling constant when $Q^2 \rightarrow \infty$ (i.e, the short distance limit) is referred to as the "asymptotic freedom". Consequently, at very large temperatures and/or densities usually achieved in heavy ion collision, the interactions which confine quarks and gluons inside hadrons should become sufficiently weak to realize the partons (quarks and gluons) as free particle in a nuclear dimension. The phase in which quarks and gluons are deconfined is termed as Quark Gluon Plasma (QGP) [6]. In QGP

, a long range colour force is Debye screened due to collective effects similar to the case of electromagnetic plasma [7]. Thus, in QGP volume the quarks interact via a short range, weak potential and consequently they tend to behave as almost free and deconfined particles after a critical value of temperature and /or density is achieved. The transition from colour insulating hadronic matter to colour conducting QGP is a new kind of phase transition since these two states of matter are very much different in nature.

On the other hand, when $Q^2 \to \infty$, QCD can be calculated perturbatively in high momentum transfer or short distance approach (pQCD) while for $Q^2 = \Lambda^2_{QCD}$, QCD is non-perturbative. In the strong coupling case, pQCD doesn't apply and some other methods may become essential, like Lattice QCD [8, 9] to describe the QCD dynamics.

1.1 Quark Gluon Plasma and Heavy Ion Collisions

QCD predicts that the quarks and gluons are confined in the hadrons in the normal conditions while a new form of matter, the quark-gluon plasma (QGP), dominated by quark and gluon degrees of freedom can be formed by heating and/or compressing normal nuclear matter. The QGP exists in early Universe, when the universe was only a few tens of microseconds old. On the other hand, a compact star, such as neutron star, is much cooler than the QGP, but it is compressed by its own weight to such high densities that it is reasonable to imagine that quark matter can again exist in the core. Experimentally, QGP can be created by "*heating*", i.e. by depositing energy into the colliding system. A unique experimental tool to reproduce the similar environment is to collide two heavy ions at very high energy. One expects to create matter under conditions that are sufficient for deconfinement. The heavy ions are accelerated and collided in the relativistic heavy ion collider, that are designed to search for the new form of matter i.e. QGP. By colliding two nuclei at different energies, we can produce hot dense nuclear matter at various temperatures (T) and baryon chemical potential

(μ_B). Hence, it allows us to access the different regions of the QCD phase diagram in order to search for the QCD critical point and to map the first order phase transition boundary. Initially in 70s and early 80s some accelerators used for particle physics were converted to accelerate heavy ions such as Bevatron at the Berkeley Lab. At the same time the energies of the accelerators used for nuclear research increased, such as in NSCL/MSU and GSI in Darmstadt. By the mid 80's the heavy ions were injected into some of the highest energy proton accelerators also, i.e. Alternating Gradient Synchrotron (AGS) at Brookhaven National Laboratory (BNL), and the Super Proton Synchrotron (SPS) at the European Center for Nuclear Research (CERN). By the early 90s the injection of the heavy ions was at the planning phase of new accelerators, like Relativistic Heavy Ion Collider (RHIC) at BNL and Large Hadron Collider (LHC) at CERN. RHIC has successfully performed Au+Au and Cu+Cu collisions at $\sqrt{s_{\rm NN}}$ = 200 GeV, which is the designed top energy for heavy ion collisions at RHIC. In 2010, Pb+Pb head on collisions at $\sqrt{s_{\rm NN}}$= 2.76 TeV were performed by LHC at CERN.

Fig. 1.2 shows a space-time evolution of the matter formed in a relativistic heavy ion collisions. Because of the Lorentz contraction effect in the moving direction, two nuclei can be seen as two thin disks approaching each other at high velocity. The energy density estimated with the Bjorken approximation for Au+Au central collision at RHIC top energy ($\sim 5\ GeV/fm^3$) is much higher than the energy density expected for the formation of QGP from the Lattice QCD calculation ($\sim 1\ GeV/fm^3$) [44].

The physics processes at the initial stage ($\sim 1 fm/c$) are dominated by hard scatterings, such as quark pair production, jet production and fragmentation. During the initial stage of the collisions, heavy ions deposit their energy into the collision region and hadrons "melt" into quarks and gluons to form QGP. The subsequent processes are the expansion and hadronization of QGP, when the fireball cools down and partons are hadronized into hadrons (1 $\sim$ 10 fm/c) also. Then, the system reaches a stage called the chemical freeze-out, where the abundance of hadrons are fixed and the inelastic interaction between hadrons ceases. Finally, the system is dilute enough and comes to

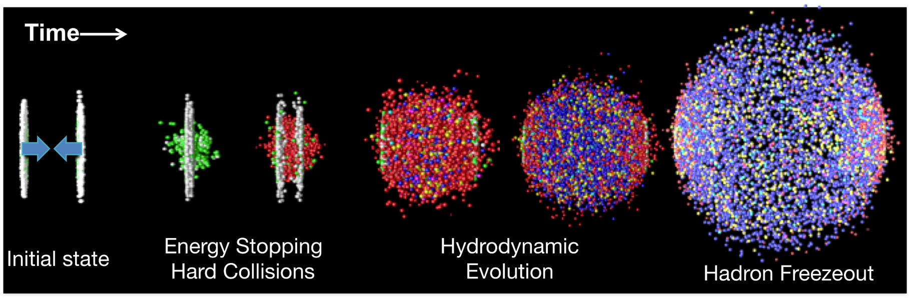

Figure 1.2: Time-evolution of a heavy ion collision. Nuclei approach each other at the speed of light and collide, creating new matter in the process. The new matter expands and cools as a fluid, eventually freezing into particles.

the kinetic freeze-out at an end, when hadrons cease their elastic interactions (10∼15 fm/c). Plenty of exciting physics results reveal that the matter created at RHIC top energy is quite different from what we observed before and it can not be described by hadronic degrees of freedom. Those measurements provide strong hints that the strongly interacting QGP has been formed at top energy of Au+Au collisions at RHIC [44].

1.2 QCD Phase Diagram and Critical Point

A lot of progress has been made recently to understand the QCD phase transition but most of the things are still not clear and there are many unanswered questions in this field, e.g., the relation between deconfining and chiral symmetry restoring phase transition, position of critical point (CP) in the phase diagram and its properties, and the signals for detection of QGP formation. The studies about QGP at baryo chemical potential $\mu_B \sim 0$ (RHIC and LHC) help us in our understanding early stages of the Universe after the Big-Bang. Similarly the properties of dense matter are needed to understand the inner core of neutron stars, where one finds μ_B very large.

1.2.1 Conjectured QCD Phase Diagram

A phase diagram mainly gives the information about the location of the phase boundaries (phase transitions) as well as the physics of the phases that these transitions delineate. Phase transitions involve thermodynamic singularities of the system. According to the Ehrenfest classification [10], a phase transition is of first-order, if at least one of the first derivatives of the grand canonical potential is discontinuous, and of second order if the first are continuous but the second derivatives are not. Thus in a first order phase transition the discontinuous first derivative can usually serve as an order parameter. According to Landau [11], a first order phase transition is defined by the appearance of different phases in coexistence, which can be distinguished and are characterised by order parameters. The appearance of latent heat is a signature of first order phase transition.

Fig. 1.3 presents the schematic phase diagram of water. The control parameters in this case are temperature (T) and pressure (P). Three regions correspond to ice, water and the steam phases. The solid lines mark the various co-existent curves, where two phases are in equilibrium.

Two special points in the phase diagram are the *triple point* ($T_{tr} = 273.16$ K, $P_{tr} = 600\ Nm^{-2}$), where all three phases co-exist and the critical point or more clearly called as *critical end point* ($T_c = 647$ K, $P_c = 2.21 \times 10^7\ Nm^{-2}$), where the meniscus separating liquid and vapour disappears and the two phases become indistinguishable. For $T < T_c$, the transition between liquid and vapour is *first-order*, implying discontinuities in entropy and volume.

At the critical end point (CEP), the transition becomes *second order*, which means that the singularity instead occurs in specific heat (C_P) and isothermal compressibility

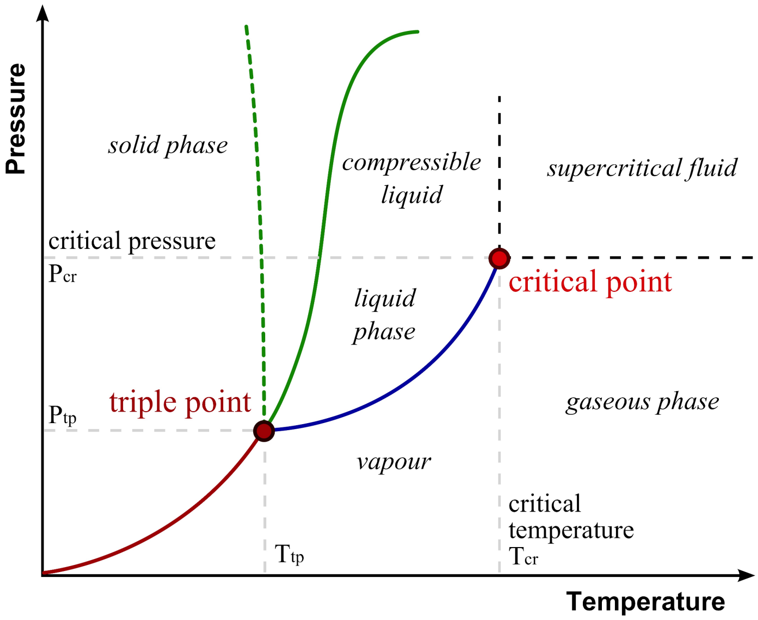

Figure 1.3: Schematic phase diagram of water in the pressure-temperature ($P - T$) plane.

(κ_T) of the fluid, which are related to the second derivative of the free energy :

$$
\begin{aligned}
C_P &= -T\left(\frac{\partial^2 G}{\partial T^2}\right)_P \\
\kappa_T &= -\frac{1}{V}\left(\frac{\partial^2 G}{\partial P^2}\right)_T
\end{aligned}
\tag{1.3}
$$

Therefore, C_P and κ_T diverges at CEP. Just beyond the CEP, thermodynamic observables still vary very rapidly. This is known as the *crossover region*.

Fig. 1.4 shows the conjectured (or proposed) QCD phase diagram in the $T - \mu_B$ plane. There should be at least three fundamental states of matter in QCD [12] : In low density and low temperature region, we have the hadronic phase with broken chiral symmetry, in which quarks and gluons are confined inside hadrons. On the other hand, in high density and high temperature region, the confinement breaks down and deconfined quarks and gluons become relevant degrees of freedom. This phase is known as

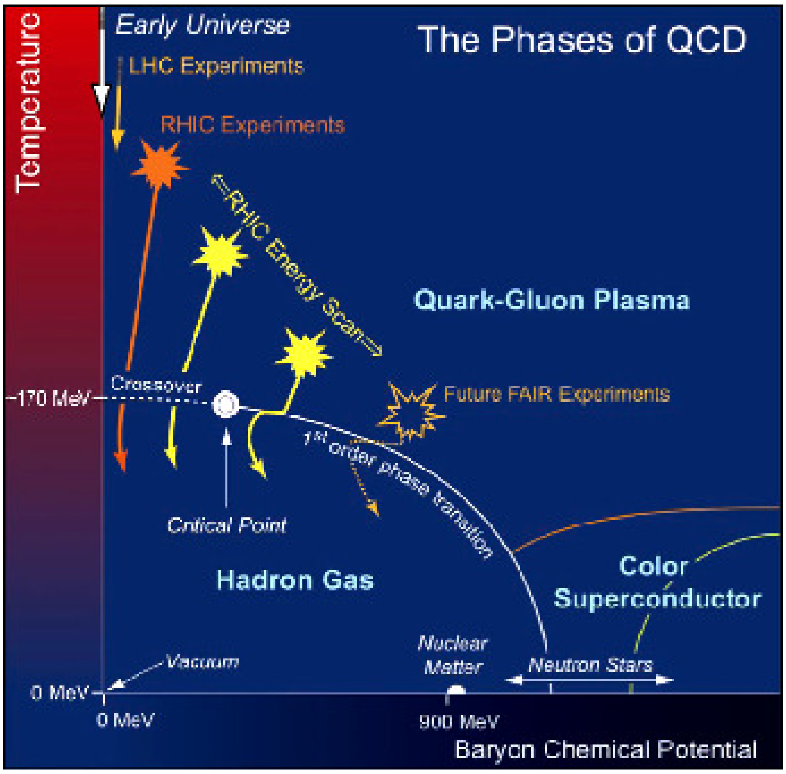

Figure 1.4: Conjectured QCD phase diagram in $T - \mu_B$ plane [13]

QGP. The third conjectured phase is a colour superconducting phase at low temperature and high μ_B.

1.2.2 QCD Critical End Point

The temperature driven transition at zero $\mu_{\rm B}$ has been studied extensively by lattice QCD techniques. Recent lattice calculations on the basis of the staggered and Wilson fermion indicate a rapid crossover from the hadronic phase to the QGP phase for realistic u, d and s quark masses [14, 15]. The pseudo-critical temperature $\rm T_c$, which characterizes the crossover location lies in the range $150-200$ MeV as shown in Fig. 1.4. The μ_B driven transition at zero T is a first order phase transition. This conclusion is less robust, since the first principle lattice calculations are not controllable in this regime due to a notorious sign problem at finite μ_B [16]. Nevertheless, a number of different model approaches indicate that the transition in this region is strongly first order. However, most of these models are essentially extensions of the linear sigma model, such as the Nambu model with or without Polyakov loop dynamics, and small modifications may alter the conclusions.

Since the first order line originating at zero T cannot end at the vertical axis $\mu_B = 0$, the line must end somewhere in the midst of the phase diagram. This end point of a first order phase transition line is a critical end point (CEP) of the second order. This is the most common critical phenomena in condensed matter physics. CEP in the proposed QCD phase diagram has much importance to understand the critical (or non-perturbative) nature of the strongly interacting matter and its governing theory, QCD. If the critical end point exists, the correlation length of an order parameter, ξ , diverges and thermodynamic quantities have singular behavior at the point, like the specific heat at the liquid-gas critical end point. Due to such singularity, the critical end point is expected to be useful for the experimental probe of the QCD phase structure in the relativistic heavy ion colliders.

Theoretically, finding the coordinates (T, μ_B) of the CEP is a well-defined task. We need to construct the partition function of QCD and to find out the singularity corresponding to the end of the first order phase transition line. But this procedure is severely impaired by the notorious sign problem in lattice calculations. Thus, nature guards its secrets better at finite μ_B and, therefore, to find the exact location of CEP, which involves finite value of μ_B, is a tedious task for the theoreticians. Certain methods were proposed to circumvent this problem [19]. However, the results obtained from different methods are quite different from each other as shown in Fig. 1.5. Thus lack of an unanimous method to circumvent the sign problem still poses a tough challenge in the search of exact location of CEP.

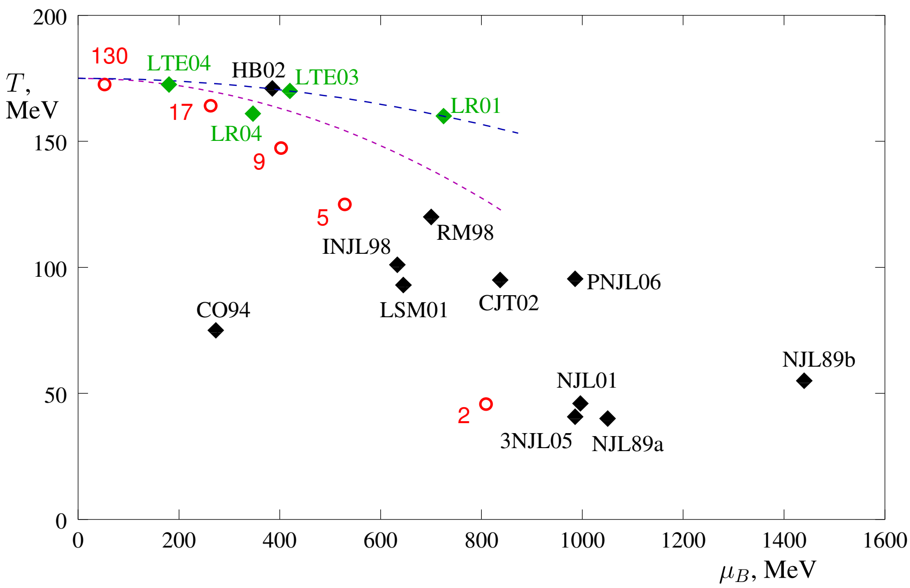

Figure 1.5: Comparison of predictions for the location of the QCD critical point on the phase diagram [18] by different theories.

1.3 QCD Critical Point: A Brief Experimental Overview

Relativistic heavy ion collision (HIC) provides a tool to realize a high energy density environment in order to study the signatures for different phases of strongly interacting matter and location of CEP as suggested by the conjectured QCD phase diagram [20]. In nuclear collisions, we expect the occurrence of high energy density in two different ways: in the "stopping regime" at a laboratory beam energy $\leq$10 GeV/A, where A is the number of nucleons in the colliding nucleus; and in the "central rapidity regime" at a beam energy $\geq$100 GeV/A. The medium formed in the stopping regime is a baryon-rich plasma, because when the nuclei are stopped together, the baryon density is found to be very large. However, at higher energies, the nuclear transparency increases and nuclei almost pass through each other, leaving an excited vacuum behind them. The energy thus trapped may become liberated in the form of multiple pion production. This region is called pionization region or the central rapidity region and has a very

Table 1.1: Past, current and future accelerator experiments for heavy ion collisions:

Accelerator	Collision Energy in CM Frame	Colliding Nuclei	Starting year
AGS (BNL, 1986)	$\sim$ 5 AGeV	p+A, O+A, Si+A, Au+Au	1986
SPS (CERN, 1986)	17.3 AGeV, 19.4 AGeV	Pb+Pb p+A, S+U	1986
RHIC (BNL, 2000)	200 AGeV, 62.4 AGeV, 130 AGeV	p+p, d+Au, Cu+Cu Au+Au,	2000
LHC (CERN,2008)	5.5 ATeV	p+p, p+Pb,	2009
CBM (GSI)	3.97 AGeV, 8.1 AGeV	p+p, p+Au, Au+Au, Pb+Pb	2018

small baryon content. In this region, hadrons are formed mainly because of the quark anti-quark pairs and gluons, and thus the medium formed is almost baryon-free. For the intermediate colliding energies, the medium formed lies somewhat in between the stopping and transparent regimes. Thus we can say that by using different kind of heavy ion collisions in the laboratory, we can form different types of media, which thus probe the various aspects of phases of QCD matter. Table 1.1 gives a summary of the accelerators, collision energy in center-of-mass frame and the colliding nuclei used for heavy ion collisions. The HIC at LHC and higher RHIC energies attempts to create a high temperature and quite dense medium which is more suitable for the possible formation of quark-gluon plasma phase and the crossover region between HG to QGP phase (as predicted by lattice QCD calculations). Complementary to these HIC experiments, CBM at GSI will shed light on the high baryon-dense medium in the stopping regime. The created medium can thus provide a way to study the various phase structures (e.g., colour superconductor phase, QCD critical end point, quarkyonic phase etc.) at high-baryon density of the conjectured phase diagram.

Experimentally, search for the QCD critical point and its signatures have been undertaken from SPS to RHIC experiments. In NA49 experiment, transverse momentum fluctuation, Φ_{p_T}-measure [21, 39], and the particle multiplicity fluctuation (the scaled variance) [38], ω, are used. In this experiment, central Pb+Pb collisions are studied at 20A, 30A, 40A, 80A, and 158 AGeV collision energy. Both Φ_{p_T} and ω, measure of transverse and particle multiplicity fluctuations, show no increase or non-monotonic behavior [38, 39] as a function of collision energies. The system size dependance of the above fluctuations are also studied for intermediate system C+C and Si+Si interaction at 158 AGeV. The higher moments of p_T fluctuation, $\Phi^{(n)}{}_{p_T}$, have also been studied to amplify the signal of the critical point in the above colliding system. No critical point signature has been found in these results. Besides, it was suggested that particle ratio fluctuation might also provide the signature of critical point because hadron production at freeze-out carry the nature of the deconfinement phase transition.

The NA49 [40] and STAR [41] experiments have also analyzed the data for dynamical fluctuation, σ_{dyn}, for the particle ratio like K/π, p/π, and K/p. In this case, the difference of the width of the particle ratio fluctuation for data and that of the mixed events are considered the dynamical fluctuation of particle ratio. These results show no non-monotonic behavior as a function of the beam energies. The NA49 intermittency result shows some clue for the presence of QCD critical point. In this analysis, second factorial moments, F_2, of low-mass $\pi^+\pi^-$ pair in central Si+Si interaction at 158 AGeV (which is $\sqrt{s_{\mathrm{NN}}}$= 17.8 GeV) are studied. The magnitude of the net-proton and σ field are characterized by the order parameter for the second order phase transition associated with QCD critical point. In this case, difference of F_2 between data and mixed events, $\Delta F_2(M)$, as a function of transverse momentum space of bin, shows intermittency signal in the data. The intermittency results for the Si+Si system approaches the QCD critical point prediction [43]. These results provide strong evidence for existence of the critical point in the proximity of the Si+Si and Pb+Pb freeze-out state. Future experiments like NA61/SHINE [42] at the CERN SPS, which is the successor of the NA49 experiment, is a dedicated experiment for the search of the critical point, whereas the RHIC beam energy scan program aims to probe the QCD critical point in a wide range of temperature and baryon chemical point. Future colliders like JINR NICA (3 GeV< $\sqrt{s_{NN}}$ <9 GeV) and GSI FAIR (2.3 GeV< $\sqrt{s_{NN}}$ <8.5 GeV) have also planned of the search for QCD critical point at low temperature and high baryochemical potential.

Chapter 2

Kinematics and Collision Dynamics

In high energy physics, we use different kinematic variables and units, which are discussed briefly in the following section along with collision pictures for heavy ions.

2.1 Kinematic Variables

We start out by looking at the global coordinate system (x,y,z), which is centered around the interaction vertex. The z-axis is chosen along the beam line, and the x-axis always points towards the center of the accelerator ring, thus leaving the y-axis to point vertically upwards. Local coordinate system (x', y', z') exists in each sub detector, with the z′-axis pointing away from the original collision. The y′-axis of the local system is parallel to the y′-axis of the global system. A sketch of these systems is shown in Fig. 2.1.

The momenta of the created particles, are split into a longitudinal component p_Z, along the beam-line and a transverse momentum component, p_T, orthogonal to the beam. The transverse momentum, illustrated in Fig. 2.1, is given by:

$$p_T = \sqrt{p_x^2 + p_y^2} \tag{2.1}$$

Similarly the transverse mass is defined as:

$$m_T = \sqrt{m^2 + p_T^2}, \tag{2.2}$$

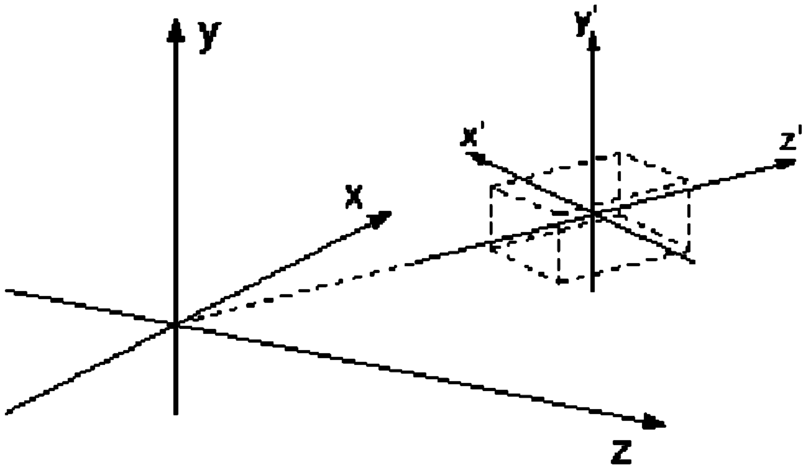

Figure 2.1: Sketch of the coordinate system used in accelerators. Collision occur at (0, 0, 0) in the global XYZ system. The Z-axis follows the beam line, and the X-axis point to the center of the accelerator ring.

Both the transverse mass and momentum are Lorentz invariant making them excellent variables in relativistic systems. The normal velocity is non-linear in successive Lorentz transformation. However a new variable rapidity, y, defined as:

$$y = \frac{1}{2} \ln \frac{E + p_z}{E - p_z}, \tag{2.3}$$

is additive under Lorentz transformation. This leaves the shape of the rapidity spectra invariant.

$$E^2 = p^2 + m^2. \tag{2.4}$$

If the mass is unknown as is the case in experiment the pseudo rapidity η is a very useful quantity, defined as:

$$\eta = -\ln \tan \theta/2 \tag{2.5}$$

θ denotes the polar angle between the momentum vector, p, and the beam axis, as seen in Fig. 2.2. In the relativistic case when p >>m the rapidity variable reduces to the pseudo rapidity variable as:

$$y = \frac{1}{2}\ln\frac{E+p_z}{E-p_z} \approx \frac{1}{2}\ln\frac{p+p_z}{p-p_z} = \frac{1}{2}\ln\frac{1+\cos\theta}{1-\cos\theta} = -\ln\tan\theta/2 \tag{2.6}$$

Here as p >>m, $E \approx p$ and $p_z = p\cos\theta$. For studying the particle production it is useful

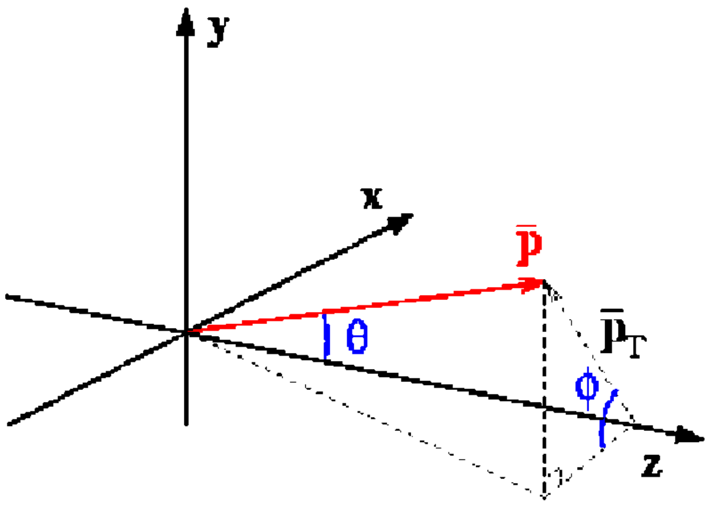

Figure 2.2: Pictorial representation of angle θ and ϕ in real experiment.

to express the invariant cross section $E\frac{d^3\sigma}{dp^3}$ in terms of rapidity, transverse momentum and the azimuthal angle ϕ, which are defined as $p_x = p_T\cos\phi$ and $p_y = p_T\sin\phi$. Using the definition of $\cos y$:

$$\begin{aligned}
\cosh y &= \frac{1}{2}(e^y + e^{-y}) \\
&= \frac{1}{2}\left(\sqrt{\frac{E+p_z}{E-p_z}} + \sqrt{\frac{E-p_z}{E+p_z}}\right) \\
&= \frac{1}{2}\left(\frac{E+p_z+E-p_z}{\sqrt{E^2-p_T^2}}\right) \\
=> E &= m_T\cosh y
\end{aligned}$$

In a similar fashion one obtains longitudinal momentum p_z as:

$$p_z = m_T \sinh y \tag{2.7}$$

To convert from usual Cartesian coordinates (x,y,z) to that used in high energy physics, *i.e.* (y, p_T, ϕ), one uses

$$f(p_x, p_y, p_z) = J f(y, p_T, \phi) \tag{2.8}$$

here, Jacobian J is defined as,

$$J(y, p_T, \phi) = \frac{\partial(p_x, p_y, p_z)}{\partial(y, p_T, \phi)} \tag{2.9}$$

now, to get Jacobian, J in Eq. 2.9,

$$J \equiv \begin{vmatrix} \partial p_x/\partial y & \partial p_x/\partial p_T & \partial p_x/\partial \phi \\ \partial p_y/\partial y & \partial p_y/\partial p_T & \partial p_y/\partial \phi \\ \partial p_z/\partial y & \partial pz/\partial p_T & \partial p_z/\partial \phi \end{vmatrix} \tag{2.10}$$

$$= \begin{vmatrix} 0 & \cos\phi & -p_T \sin\phi \\ 0 & \sin\phi & p_T \cos\phi \\ -E & \partial p_z/\partial p_T & \partial p_z/\partial \phi \end{vmatrix} \tag{2.11}$$

$$= E.p_T$$

The rapidity variable has the useful property that it transforms linearly under a Lorentz transformation so that the invariant cross-section is given by:

$$E\frac{d^3\sigma}{dp^3} = \frac{d^2N}{2\pi p_T dp_T dy} = \frac{d^2N}{2\pi m_T dm_T dy} \tag{2.12}$$

Here the integration over the azimuthal angle gives the factor of 2π. The right hand side of equation 2.12 ,This is a very important observable in heavy ion physics and is used to study particle yields. From experimental consideration, normalizing by the number of events one uses,

$$E\frac{d^3\sigma}{dp^3} = \frac{1}{N_{event}}\frac{d^2N}{2\pi p_T dp_T dy} \tag{2.13}$$

Where, N is the measured number of a given particle species, and N_{event} is the number of events. In the following sections an introduction to the central pictures and concepts of relativistic heavy ion collisions is given.

2.2 Collision Picture

In Fig. 2.3 an illustration of a relativistic collision is shown as seen from the Center-of-mass frame of the nuclei. Each nucleus is Lorentz contracted along its direction of motion.

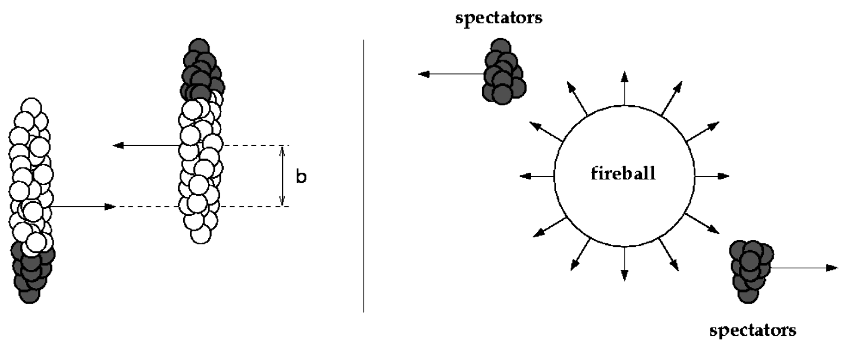

Figure 2.3: Schematic illustration of a relativistic heavy ion collision. The participant nucleons of the overlap region between the colliding nuclei form the high density fireball, whereas the rest of the nucleons continues unaffected as spectators.

2.2.1 Participants and Spectators

The nucleons directly involved in the collision, called participants, interact strongly giving rise to a high density volume, known as the fireball. Nucleons outside the overlapping region of the two nuclei are called spectators. They are unaffected by the collision except for Coulomb-interactions and they retain their initial momentum, flying away from the fireball. Fig 2.3 also introduces the impact parameter, b, which is the transverse distance between the centers of the two nuclei. A large impact parameter hence corresponds to a peripheral collision, where a small region of the nuclei overlap, whereas a small impact parameter gives a central collision with a large overlapping region and hence more number of nucleon participants. As it is practically impossible to measure the impact parameter directly, an experimental technique is used to distinguish collisions into classes of centrality. This is done based on the multiplicity or transverse energy of the events so that the collisions with highest particle production are defined as most central.

The impact parameter is correlated to the centrality of the collision in the following way:

$$c = \frac{\int_0^{b_c} \frac{d\sigma_{in}(b')}{db'} db'}{\sigma_{in}} \tag{2.14}$$

Here σ_{in} ,$d\sigma_{in}(b')/db'$ and b_c are the total inelastic nuclear reaction cross section, the differential cross section and a cut-off in the impact parameter, respectively. Thus the centrality, c, denotes the probability that a collision occurs with an impact parameter of $b \leq b_c$. For a solid sphere $\frac{d\sigma_{in}(b')}{db'} = 2\pi b db$ and thereby under the assumption that nuclei are identical and spherical the centrality becomes:

$$c = \frac{\int_0^{b_c} 2\pi b db}{\int_0^{2R} 2\pi b db} = \frac{b_c^2}{4R^2}$$

Here R denotes the radius of the nuclei. Consisting of 197 nucleons, Au is found to have $R = R_0 A^{1/3} = 1.2197^{1/3} fm = 7.0 fm$. R_0 is taken as 1.2 fm. The impact parameter and the number of participants in the collision are directly related. Their relation can be estimated using the Glauber model.

2.2.2 The Bjorken Picture

A important contribution to heavy ion physics is a paper from 1983 by Bjorken , which deals with a hydro-dynamical description of the central rapidity region in heavy ion collisions. The description depends on four important assumptions on collisions between nuclei with number of nucleons A:

• **Boost in-variance**: Each thin slab (perpendicular to the z-axis) of the fireball is boost invariant; hence there will be no longitudinal pressure gradient. The energy density and particle production for any given slab will then be the same, so the total particle production as a function of rapidity dN/dy (also boost invariant), will have a plateau shape. This however is only assumed to be true in a few units of rapidity around mid-rapidity.

• **Transparency**: The nuclei interpenetrates in the Au+Au collision and the central plateau is formed through particle production from the breaking of colour strings. The fragments of the original nuclei end up some units of rapidity from mid-rapidity. In Lorentz frames with velocities close to the mid-rapidity frame, the nuclei look like flat pancakes.

• **Transverse expansion**: The radial expansion is negligible compared to longitudinal. The fireball will thus appear to be stretched out between the two incident nuclei, so for central collisions it takes on a cylindrical form. This is assumed to hold good at least until some time after possible QGP is formed.

• **Thermalization**: At some early time, assumed to be of the order of the characteristic hadronic time scale t∼1 fm/c, the system thermalises and hydrodynamics governs the evolution and expansion of the source.

These assumptions lead to a diagram of the space-time evolution of the post-collision dynamics. If the longitudinal expansion of the nuclei is neglected, assumption 1 gives that all slabs move according to:

$$z = \beta t \tag{2.15}$$

and have a proper time:

$$\tau = \frac{t}{\gamma} = \sqrt{t^2(1 - \frac{z^2}{t^2})} = \sqrt{t^2 - z^2} \tag{2.16}$$

As each slab is unaffected by neighboring slabs (assumption 1), they can be seen as evolving independently in their own proper time. The proper time forms a hyperbola in (z,t) plane, which is shown in Fig. 2.4.

In the Bjorken picture the incoming nuclei are transparent to each other as mentioned, allowing them to interpenetrate without loosing much of their initial kinetic energy. However, upon doing so they leave a highly excited colour field between them, in which particle production take place due to the breaking of colour strings. The concept of transparency is illustrated in Fig. 2.5.

2.2.3 The Landau Picture

The intuitive understanding of a collision would be that the two particles collide and lose all of their kinetic energy in the process, like any two macroscopic massive objects. This was also the first approach proposed by Landau in 1953. The Landau picture consists of 3 stages:

• **Full stopping**: When the two nuclei collide all energy is released and many particles

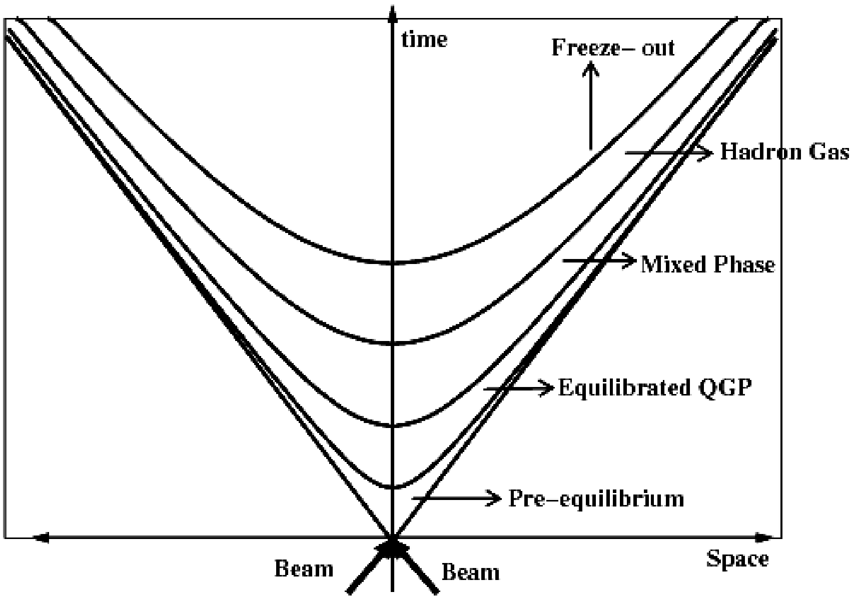

Figure 2.4: Proposed space-time evolution of a heavy ion collision. Quarks and gluon are at first deconfined in a QGP which thermalises; eventually the hadrons freeze out and streams away freely [17].

are instantly created from the collision overlap area. The mean free path is so small that the system is instantly in statistical equilibrium.

• **Hydrodynamics**: The system expands according to relativistic hydrodynamics with the strong force being the only interaction. The fireball is assumed to be an ideal fluid, that is, it has no viscosity and thermal conductivity. Particles are still being created and absorbed since the energy density is above the chemical potential for many particles.

• **Adiabatic expansion**: The fluid expands adiabatic-ally, i.e. the entropy is constant. As the system expands, the mean free path increases and energy density decreases. At a critical time, no particles or very few are scattered or created. Landau named it as the "break-up stage", but it has later been renamed as "freeze-out".

An interesting point is that the original baryons (nuclear fragments) have no " special qualities " in the fireball, and as it expands and freezes out, the fragments will be distributed according to relativistic hydrodynamics like the other particles. A collision in accordance with the Landau picture is illustrated in Fig. 2.6.

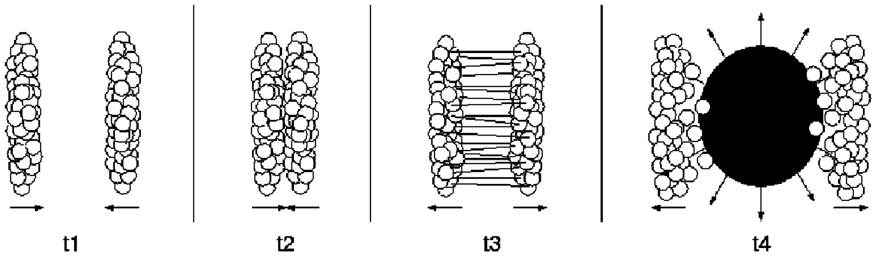

Figure 2.5: Schematic view of a collision in the transparent (baryonless mid-rapidity) picture.

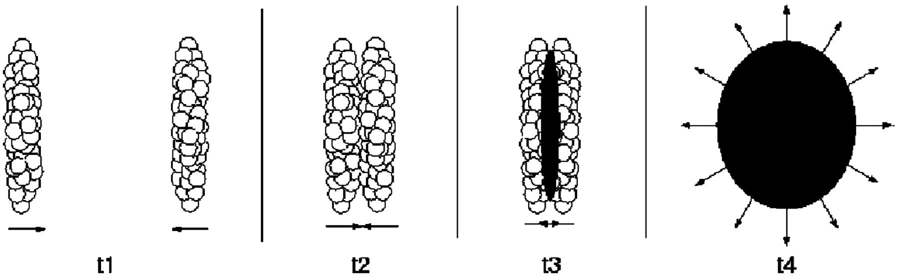

Figure 2.6: Schematic view of a collision in Landau's nuclear stopping picture.

These two extreme pictures corresponds to very different macroscopic physical phenomena. The transparent Bjorken picture is reminiscent of the early Universe, with very high temperature and low baryon-chemical potential, μ_B. In the other end of the scale, Landau's stopping picture is reminiscent of the conditions inside stellar objects like neutron stars, with large μ_B and relatively low temperature. At RHIC, it is found by nuclear stopping measurements, that the higher the collision energy is, the more transparent the collision is.

Chapter 3

Baryon Stopping in High Energy Nuclear Collisions

The characterisation and interpretation of the proton distributions produced in heavy ion collisions are important to understand the dynamics of hot and dense nuclear matter. It can be observed from the nuclear matter phase diagram shwon in Fig. 1.5, there exists a continuum of critical temperatures and baryon densities at which a phase transition from a hadron gas to a Quark Gluon Plasma (QGP) might occur. By studying stopping in heavy ion collisions as a function of beam energy, we are able to determine whether the energy densities attained in the collisions are high enough to allow a phase transition to a QGP state.

We know the initial (pre-collision) and final states of the proton distributions as a function of rapidity. There are two distinct signatures, which may be inferred from the observed proton rapidity densities: incomplete stopping/nuclear transparency and longitudinal hydrodynamic flow. While the true situation is a combination of these two effects, they cannot be easily disentangled. In the following sections, the interpretations of the observed proton rapidity densities at AGS (2, 4, 6 and 8 AGeV) and RHIC (62.4 and 200 GeV) are discussed.

3.1 Nuclear Stopping

Landau and Bjorken models, each composed of two extreme nuclear collision cases: total nuclear stopping and transparency, respectively. Experiments have been trying to look for signatures, which reveals the collision dynamics and the created new form of matter. This might be good to explore the collision dynamics, which in turn can be used to validate and improve theoretical models.

The nuclear stopping power is a measure of the degree to which the kinetic energy of the relative motion of the two colliding nuclei is transformed into other degrees of freedom. As the nuclear stopping increases, thermalization of incident energy increases and high energy density is observed. The production of particles will increase and a collective flow is expected.

3.1.1 Quantifying Baryon Stopping in High Energy Nuclear Collisions

A baryon is a tri-quark bound state (e.g. proton, neutron, hyperon, etc.), and the corresponding quantum number (called the baryon number denoted B) is +1 for a baryon and -1 for an anti-baryon or ± 1/3 per (anti)quark, all other particles (fundamental or bound state) have B=0. It is empirically observed that in any interaction, either elastic or inelastic, the total baryon number is conserved.

Experimental Consideration

In heavy ion collisions, two nuclei moving at relativistic speed deposite their kinetic energy in small region for a short time of interval for the possible formation of QGP and the particle production. The mean rapidity loss is a measure of kinetic energy loss quantified as

$$\delta y = y_p - < y_{net-b} >, \tag{3.1}$$

here y_p is the rapidity of the beam protons and $\langle y_{net-b} \rangle$ is the mean rapidity of net-baryons after the collisions. Net-baryon is defined as the number of baryons minus the number of anti-baryons. Experimentally it is not possible to distinguish between the produced and those originating from collision remnants. To extract the pure collision remnants rapidity distribution from experimental data, different phenomenological models have been used.

Rapidity losses in heavy ion collisions are measured at different center of mass energies at AGS, SPS to RHIC [29] [32] [26] in order to determine the degree of nuclear stopping and energy density built up in the stopping region. At AGS energies, the net-baryon distributions are described with double Gaussians distributions demonstrated by the E917 collaboration.

The mean rapidity losses can be estimated by using Eq.3.1 with the $\langle y_{net-b} \rangle$, determined from the Gaussian distribution centered at positive rapidity. It is assumed that the Gaussian corresponds to projectile baryon distribution. At SPS and RHIC energies the mean rapidity losses are calculated without discriminate the origin of the net-baryons. The comparison of rapidity losses at different energies becomes complicated, when the contribution of target baryon to the net-baryon distribution at rapidity region above mid-rapidity shows a strong energy dependence [25]. Thus it is necessary to examine the sensitivity of rapidity loss to the target baryon contribution in order to study the energy dependence of the rapidity loss.

Before the collision, the projectile baryons peak at $\langle y_p \rangle$ and after the collision the projectile baryon distribution extend from target rapidity to the projectile rapidity. Thus, to obtain the average projectile baryon rapidity $\langle y_{net-b} \rangle$ after the collision, the integration is carried out from the target rapidity to the projectile rapidity. For symmetrical heavy ion collisions, $\langle y_p \rangle$ can be expressed in the center-of-mass system as:

$$< y >= \frac{2}{N_{Part}} \int_{-y_p}^{y_p} y \frac{dN_{B-\bar{B}}}{dy} dy, \tag{3.2}$$

Where $dN_{B-\bar{B}}/dy$ is the net-baryon rapidity density, which is related to the net-proton distribution and N_{part} is the number of participating baryons in the collisions. The net-baryon yield can be estimated from the net-proton yield, $i.e.$ the difference of proton and anti-protons yields. thus, the rapidity distribution of the net-protons after the collision determines the energy available for particle production and yields the information on the stopping of ions due to their mutual interactions.

In case of full stopping, the average rapidity loss is $\delta y = y_p$, which means that $< y_{net-b} >$ is 0. In case of total transparency δy= 0, because the net-baryons stay in the beam rapidity region $< y_{net-b} > = y_p$, and because of baryon number conservation, any baryons created between the nuclear fragments should be from baryon-anti baryon pair production and thus keeping the region net-baryon free.

The non-(direct) interdependence between stopping and energy loss means that a high degree of transparency doesn't necessarily mean low energy loss. This is fortunate as the transparency seem to increase with the beam energy. If this hadn't been the case, building bigger accelerators in order to increase the energy available for particle production would largely be futile.

3.2 Protons as a Proxy for Baryons

In most of the experiments the only identifiable baryons measured are protons. Neutrons are the lightest non-detectable baryons only measured in zero degree calorimeter (ZDC) for centrality selection and are most likely to be produced. However, some heavier strange baryons ($\wedge$, Σ^0,Σ^+ and Σ^-) are also produced, while they decay into either protons or neutrons before reaching the detector.

This is obviously a non-trivial problem for the measurements related to baryons. Similar is the situation in case of net-baryon susceptibilities. As net-baryon is a conserved quantity not the net-proton, therefore it has been questionable to use net-protons as a probe to look for CEP. On the other hand, since the σ-measure to quantify fluctuations in theories are blind to isospin symmetries, it is argued that the measurements of net-protons are equally good as net-baryons. Therefore proton works as a proxy of baryons in event-by-event fluctuation measurement of net-baryons.

3.3 Review of Previous Results

Stopping has been examined in several experiments at different energies and particle species. The shape of the net-baryon distribution at different energies is shown in Fig. 3.1 [26]. At AGS ($\sqrt{s_{NN}}$ = 11.6 GeV) for Au-Au collisions (y_b ~1.64) the distribution peaks at mid-rapidity and then falls off as the rapidity increases, looking mostly like a Landau Gaussian rapidity profile. But at higher energies like SPS for Pb+Pb collision at $s_{NN} = 17.2$ GeV, ($y_b \sim 2.9$) a dip is seen in the middle of the distribution. It is observed that the net-baryons have a tendency to shift forwards (and backwards). The central region does, however, contain a fair amount of net-baryons indicating a certain degree of stopping.

At 200 GeV Au-Au collisions (RHIC's top centre of mass energy) a large portion of the mid-rapidity net-baryon distribution exhibits a flattening indicating a high degree of transparency. This is much more consistent with Bjorken type of collision picture. Several models have also been employed to examine the net-baryon distribution and stopping. For some of the models, there does seem to be some agreement with the transparencies seen in the higher energy experiments. It may not be qualitatively exact, but they do appear to push the net-baryons into the forward rapidity region.

Fig 3.1 shows net–proton dN/dy measured at AGS, SPS and LHC energies. The distributions show a strong energy dependence. The net–protons peak at mid-rapidity at AGS, while at SPS a dip is observed in the middle of the distribution. At RHIC, a broad minimum has developed spanning several units of rapidity, indicating that at RHIC energies collisions are quite transparent. In Fig 3.1, all data are from the top 5 % most central collisions and the errors are both statistical and systematic (the light gray band shows the 10% overall normalization uncertainty on the E802 points, but not 15% for E917). The data have been symmetrized. For RHIC data black points are measured and gray points are symmetrized (mirror reflections about y_{cm}), while the opposite is true for AGS and SPS data (for clarity). At AGS, weak decay corrections are negligible and at SPS they have been applied.

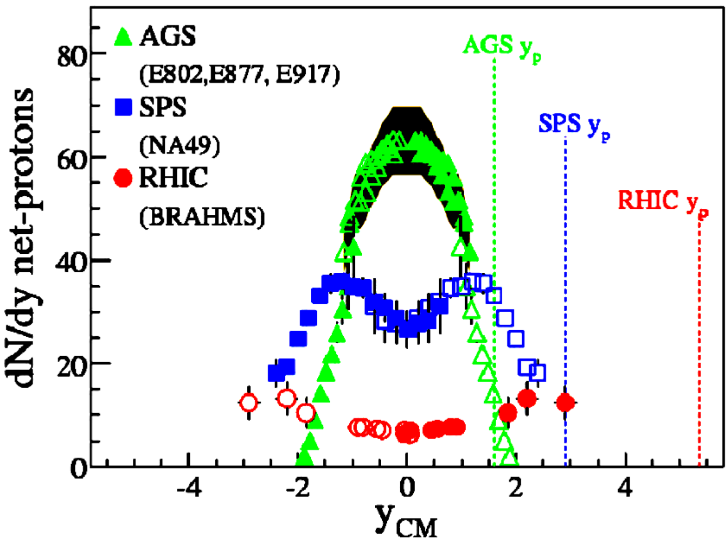

Figure 3.1: The net-proton rapidity distribution at AGS [27–29] (Au+Au at 5 GeV), SPS [32] (Pb+Pb at 17 GeV) and RHIC (Au+Au at 200 GeV). The data are from the top 5% most central collisions and the errors are both statistical and systematic. The figure is adopted from Ref. [26]

.

The energy dependence of rapidity loss

The rapidity losses can be calculated using Eq.3.1 and Eq.3.2 as a function of projectile rapidity (in the CM). Rapidity losses in heavy ion collisions were measured at different energies at AGS [32], SPS [29] to RHIC [26]. Fig.3.2 shows the rapidity loss in which $< y_b >$ was evaluated from mid-rapidity to beam rapidity. In Fig.3.2 from AGS to

SPS, avarage rapidity loss $< y_b >$ increases linearly with the beam energy y_b. When discussing at RHIC, we study the average rapidity loss at $\sqrt{s_{\mathrm{NN}}} = 62.4$ and 200 GeV, a new linear increasing relationship is established from SPS to RHIC, but this begins to increase slowly unlike the degree of increase that was observed at AGS to SPS energies.

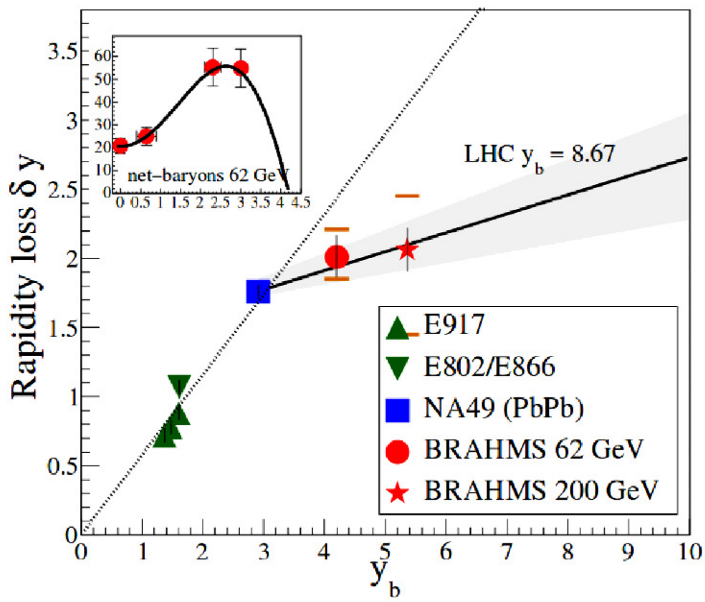

Figure 3.2: The inset plot shows the extrapolated net-baryon distribution (data points) with fits (represented by the curves) to the data. The full Fig 3.2 shows the rapidity loss, obtained using Eq. 3.2, as a function of projectile rapidity (in the CM). The figure is adopted from Ref. [26]

.

Chapter 4

Effect of Baryon Stopping on Higher Moments of Net-Proton

In recent years, using control parameters temperature (T) and baryon chemical potential (μ_B) the Beam Energy Scan (BES) program at Brookhaven National Laboratory's Relativistic Heavy Ion Collider (RHIC) has drawn much attention to map the quantum chromodynamics (QCD) phase diagram in terms of [45]. Lattice QCD calculations combined with other theoretical models suggest that there should be a critical point, where the phase transition line of first order originating from high μ_B ends [46–48]. Experimentally the location of the critical point can be measured by scanning the $T - \mu_B$ plane of the phase diagram. One can scan the $T - \mu_B$ plane by varying the center-of-mass energies of the colliding ions.

Measurement of the moments of distributions for conserved quantities like net-baryon, net-charge and net-strangeness number for systems undergoing strong interactions as in high energy heavy ion collisions, have recently provided rich physics insights [66, 67]. The most crucial realisation is that, the product of moments of the conserved number distributions are measured experimentally and can be linked to susceptibilities (χ) computed in Quantum Chromodynamics (QCD) based calculations. For example, $S\ \sigma = \chi^{(3)}/\chi^{(2)}$ and $\kappa\ \sigma^2 = \chi^{(4)}/\chi^{(2)}$, where σ is the standard deviation, S is the skewness, κ is the kurtosis of the measured conserved number distribution, $\chi^{(n)}$ are the n^{th} order theoretically calculated susceptibilities associated with these conserved numbers.

Non-monotonic variation of observables related to the moments of the distributions of conserved quantities with $\sqrt{s_{\mathrm{NN}}}$ are believed to be good signatures of a phase transition and a CEP. The moments are related to the correlation length (ξ) of the system. The signatures of phase transition or CEP are detectable if they survive the evolution of the system. Finite size and time effects in heavy ion collisions put constraints on the significance of the desired signals. A theoretical calculation suggests a non-equilibrium $\xi \approx$ 2-3 fm for heavy ion collisions. Hence, it is proposed to study the higher moments (like skewness, $S = \langle(\delta N)^3\rangle/\sigma^3$ and kurtosis, $\kappa = [\langle(\delta N)^4\rangle/\sigma^4] - 3$ with $\delta N = N - \langle N\rangle$) of distributions of conserved quantities due to a stronger dependence on ξ. Both the magnitude and the sign of the moments, which quantify the shape of the multiplicity distributions, are important to understand the phase transition and CEP effects. Further, products of the moments can be related to susceptibilities associated with the conserved numbers. The product $\kappa\sigma^2$ of the net-baryon number distribution is related to the ratio of fourth order ($\chi_{\mathrm{B}}^{(4)}$) to second order ($\chi_{\mathrm{B}}^{(2)}$) baryon number susceptibilities. The ratio $\chi_{\mathrm{B}}^{(4)}/\chi_{\mathrm{B}}^{(2)}$ is expected to deviate from unity near the CEP. It has different values for the hadronic and partonic phases. Such a connection between theory and high energy heavy ion collision experiment has led to furthering our understanding about the freeze-out conditions [50, 66], details of the quark-hadron transition and plays a crucial role for the search of possible QCD critical point in the QCD phase diagram.

The STAR experiment has measured the event-by-event proton (N_p) and anti-proton ($N_{\bar{p}}$) multiplicities for Au+Au minimum-bias events at $\sqrt{s_{\mathrm{NN}}}$ = 7.7, 11.5, 19.6, 27, 39, 62.4, and 200 GeV to calculate net-proton fluctuations. The 19.6 and 27 GeV data were collected in the year 2011 and the other energies were taken in 2010.

But, the STAR proton multiplicities include the protons from stopping, resonances and production. It is to be noted that the conservation of baryon numbers is associated to only produced protons not with the stopping ones. Therefore, in the present work, we try to estimate the stopped protons and then remove their contribution from the STAR measured proton multiplicities. Since the STAR measurement use all the protons to estimate the higher order moments of net-protons distributions, It will be constructive to check whether the non-monotonic behavior of higher moments persists by removing the stopped protons from STAR data.

4.1 Estimation of Baryon Stopping from Rapidity Distribution

The rapidity distribution of net-protons after the collision determines the available energy for particle production as well as tells about the stopping of the ions due to their mutual interaction. The net-baryon rapidity distribution is the direct measure of baryon stopping. The experimental information on neutrons is unavailable so we have to rely on proton data. Presently there exists experimental data on proton (or net-proton) rapidity spectra at AGS [27–29], SPS [32–36] and RHIC [25, 26] energies. In central Au+Au heavy ion collision at AGS energies rapidity distribution of proton indicates almost complete stopping. Nuclear rapidity distribution yield information on nuclear stopping, which provides a measure of energy that is deposited for particle production. Therefore, baryon stopping calculation is of prime interest for theoretical understanding and to connect it with experimental results.

4.1.1 Fitting Function used for Analysis of Experimental Data

In order to determine the stopping of the collision we first need the net-baryon distribution function. This means, we will have a function to fit the net-baryon distribution available at different energies. The choice of a function is however not theoretically determined, but by observing the net-baryon distribution at different energies from AGS to RHIC. we can consider a double Gaussian function so the function should be flat around mid-rapidity, increases towards higher rapidity and terminate at y_{beam}. To make this comparison more quantitative, we fit data by a simple function which has a thermal origin explained in Ref. [37]. The invariant momentum spectrum of particles radiated by a thermal source with temperature T is given as follows:

$$E\frac{d^3n}{d^3p} = \frac{dn}{dym_T dm_T d\phi} = \frac{gV}{(2\pi)^3}Ee^{-(E-\mu)/T} \tag{4.1}$$

Now, Eq. 4.1 can be written as:

$$\frac{1}{2\pi}\frac{dn}{dym_T dm_T} = \frac{gV}{(2\pi)^3}Ee^{-(E-\mu)/T} \tag{4.2}$$

or,

$$\frac{dn}{m_T dm_T dy} = \frac{gV}{(2\pi)^2}Ee^{-(E-\mu)/T}.$$

Here, g is the spin/isospin-degeneracy factor for the particle species and μ the grand canonical potential $\mu = b\mu_b + s\mu_s$ as originating from its baryon and strangeness quantum numbers b and s, respectively . For simplicity, we neglect quantum statistics with the reasoning that its influence will be rather small at the low densities where the particles typically decouple from each other and where the spectra are computed.

Volume of the source, giving together with the factor $e^{\mu/T}$ is the normalization of the spectrum, which we will always adjust for a best fit to the data, because we are only interested in the shape of the spectra to reveal the dynamics of the collision zone at freeze-out. In the remainder of the text we will always give the spectra in terms of rapidity $y = \tanh^{-1}(p_L/E)$, where $p_L \equiv$ longitudinal momentum.

Inserting $E = m_T \cosh y$ in above Eq. 4.2 and integrated over transverse component from $m_T = m$ to $m_T = \infty$, we get the total rapidity density dn/dy as follows

$$\frac{dn}{dy} = \int_{m_T=m}^{\infty} \frac{gV}{(2\pi)^2} m_T^2 \cosh y e^{-(E-\mu)/T} dm_T. \tag{4.3}$$

Now by integrating the invariant momentum spectra in Eq. 4.3 over the transverse component:

$$\frac{dn}{dy} = \frac{V}{(2\pi)^2}T^3(\frac{m^2}{T^2} + \frac{m}{T}\frac{2}{\cosh y} + \frac{2}{\cosh y^2}) \times exp(-\frac{m}{T}\cosh y). \tag{4.4}$$

For the sake of convenience in this equation we can neglect the last two terms and the equation can be written as:

$$\frac{dn}{dy} = \frac{V}{(2\pi)^2}\frac{m^2}{T^2} \times exp(-\frac{m}{T}\cosh y)$$

$$=> \frac{dn}{dy} = A(exp(-\frac{m}{T}\cosh y)). \tag{4.5}$$

Here, A is the normalization constant because m and T are independent of y so we can take them into the constant term. Since in symmetric heavy collisions both the nuclei are same and the formed fireball is a mixture of two sources, so the above function can be modified for symmetric collisions as follows [24] :

$$\frac{dn}{dy} = a(exp(-(1/w_s)cosh(y - y_{cm} - y_s)) + exp(-(1/w_s)cosh(y - y_{cm} + y_s))), \tag{4.6}$$

where a, y_s and w_s are parameters of the fit function. The Eq. 4.6 is a sum of two thermal sources shifted by $\pm y_s$ from the mid-rapidity. The width w_s of the sources is being interpreted as w_s = (temperature)/(transverse mass). Here we consider collision of identical nuclei, so parameter of the two sources are identical. These parameters monotonously rise with the energy. Baryon stopping is most directly measured via the rapidity distribution of net-proton (the number of proton minus anti-protons). At AGS, for central (0-5%) Au+Au collision production of anti-protons is very small so the net-proton distribution is same as proton distribution, the rapidity distribution is peaked at mid-rapidity. As the collision energy increases, the distribution peaks at higher rapidity.

4.1.2 Fitting Parameters

The variation of fit parameters, y_s and w_s with center-of-mass energy $\sqrt{s_{\rm NN}}$ is shown below in Fig. 4.1. Both the parameters increase monotonically with the energy and can be fitted by a exponential function.

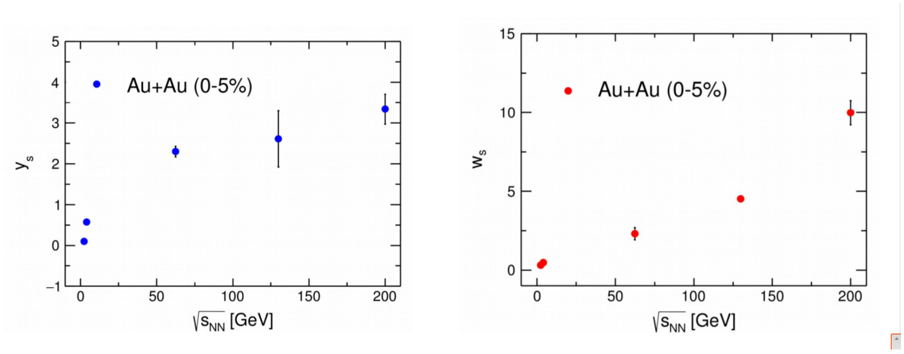

Figure 4.1: (Left panel) The shift in rapidity of two sources y_s, with center-of-mass energy $\sqrt{s_{\rm NN}}$, this shows a monotonic rise of y_s with $\sqrt{s_{\rm NN}}$. (Right panel) The width parameter, w_s, as a function of $\sqrt{s_{\rm NN}}$.

Baryon stopping, is most directly measured via the rapidity distribution of net-protons. At AGS for central (0-5%) Au+Au collisions, the production of anti-protons is very small so that the net-proton distribution is same as proton distribution and the rapidity distribution is peaked at mid-rapidity. As the collision energy increases, the distribution peaks at higher rapidity.

4.2 Calculation of Baryon Stopping using Rapidity Distribution of Protons

BRAHMS has measured the net-proton rapidity distribution at RHIC in the rapidity range of $0 < y < 3.1$ for 0-10% central collisions at $\sqrt{s_{\rm NN}}$ =62.4 GeV and 0-5% central collision at $\sqrt{s_{\rm NN}}$=200 GeV [25] [26]. Also the rapidity distributions are measured at AGS in different rapidity ranges. The distribution measured at RHIC is very different from those at lower energies, as possibly a different system is formed near mid-rapidity.

In order to calculate the stopping, we fit a function to the rapidity distribution of protons. We chose a two source fit function as given in Eq. 4.6 by observing the behaviour of the rapidity distribution at different energies. This function in Eq. 4.6 fits the rapidity distribution of proton, which is flat around mid-rapidity and increases towards higher rapidities, terminating at y_{beam}.

The fitting procedure uses ROOT's χ^2-minimization method. The χ^2/ndf or the reduced-χ^2 is found to be around 1, indicating a very good fitting of net-proton rapidity spectra to the two-source fitting function. Fit results are shown in Fig. 4.2. The rapidity densities of proton at AGS and net-proton ($p - \bar{p}$) at RHIC are from most central Au+Au collisions. Experimental data are from collaboration E802 [27], E877 [28], E917 [29], E866 [31], RHIC at 62.4 and 200 GeV.

Table 4.1: Percentage of baryon stopping at different energies from AGS and RHIC

$\sqrt{s_{\rm NN}}$	% baryon stopping
2 AGeV	64.23 ± 0.13
4 AGeV	52.16 ±0.15
6 AGeV	47.59 ± 0.12
8 AGeV	44.61 ± 0.12
62.4 GeV	4.58 ± 0.11
200 GeV	2.91 ± 0.00

We have calculated the net number of protons per unit of rapidity around $y = 0$ at AGS [27] [28] [29] and RHIC [25] [26] energies in mid-rapidity by integrating the fit function given by Eq. 4.6 in the range $-y_b$ to $+y_b$. In Fig. 4.2, the circles are data points or the resulting rapidity density dN/dy as a function of rapidity. The most prominent feature of the data is that, while the proton and anti-proton dN/dy decreases towards forward rapidities, while the net-proton dN/dy increases. A two source fitting function nicely fits to this distribution, giving the total extrapolated net-proton dN/dy at mid-rapidity at different energies, i.e stopped protons. At 2, 4, 8 A GeV stopped protons

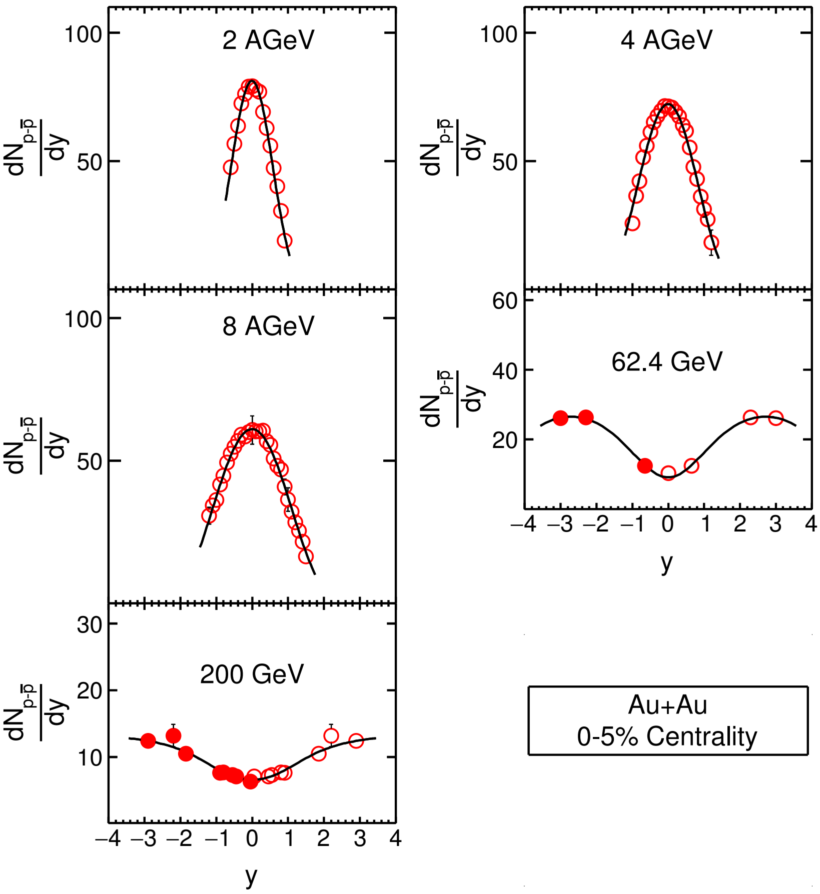

Figure 4.2: The rapidity densities of protons at 2, 4, 8A GeV (AGS) and net-proton ($p-\bar{p}$) (for RHIC energies) from central collision of Au+Au (AGS and RHIC) in center-of-mass system. Experimental data are from collaboration E802 [27], E877 [28], E917 [29], E866 [31], RHIC experiments. The open circles are experimentally measured data points and the filled circles are the mirror reflections, assuming a symmetry in particle production. Solid lines represent the two source fit function given by Eq. 4.6.

are around 72, 69, 58 in numbers and at RHIC energies for 62.4 and 200 GeV, they are around 10 and 6 in numbers respectively.

Then to calculate the percentage of stopping, we integrate the fit function in whole rapidity range. We calculate baryon stopping at AGS (2, 4, 8A GeV) and RHIC (62.4 and 200 GeV) energies. The calculated percentage of stopping at these energies are shown in Table 4.1. Now this extrapolated percentage of stopping can be fitted with an exponential fit function, which is shown in Fig. 4.3.

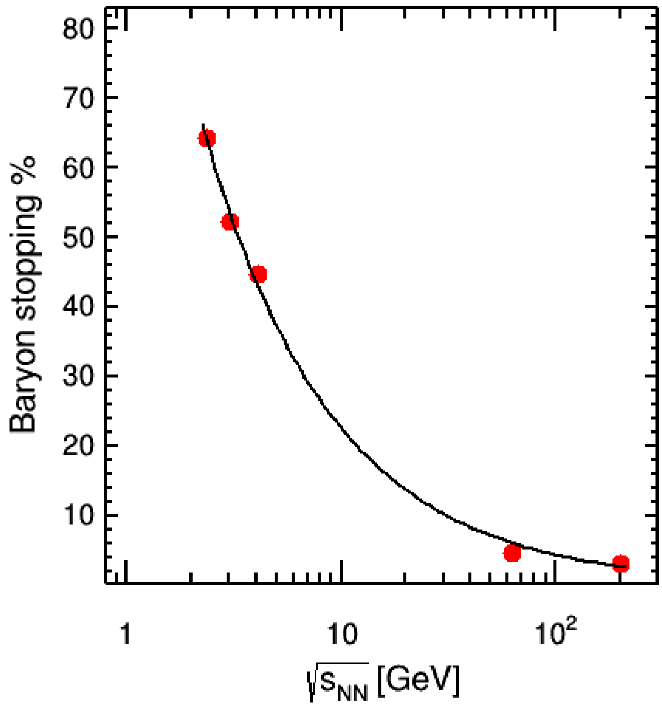

Figure 4.3: Percentage of baryon stopping as a function of $\sqrt{s_{\mathrm{NN}}}$, showing an exponential decrease with energy.

Afterwords, we parameterise the baryon stopping percentage as a function of $\sqrt{s_{\mathrm{NN}}}$ with an exponential function to get a parametric form. Using this function, we interpolate the percentage stopping at STAR BES energies for $\sqrt{s_{\mathrm{NN}}}$= 7.7, 11.5, 19.6, 27, 39, 62.4, 200 GeV, which is crucial to study the CEP. The calculated percentage

Table 4.2: Percentage of baryon stopping at different STAR BES energies:

$\sqrt{s_{\mathrm{NN}}}$ [GeV]	7.7	11.5	19.6	27	39	62.4	200
Baryon Stopping [%]	27.27	20.43	13.90	11.03	8.46	6.03	2.60
No. of stopped protons	18.79	14.02	9.73	7.61	5.78	3.78	1.544

of stopping at STAR BES energies are shown in Table 4.2. For STAR BES energies $\sqrt{s_{\mathrm{NN}}}$ = 7.7, 11.5, 19.6, 27, 39, 62.4, 200 GeV, the percentage of Baryon stopping is

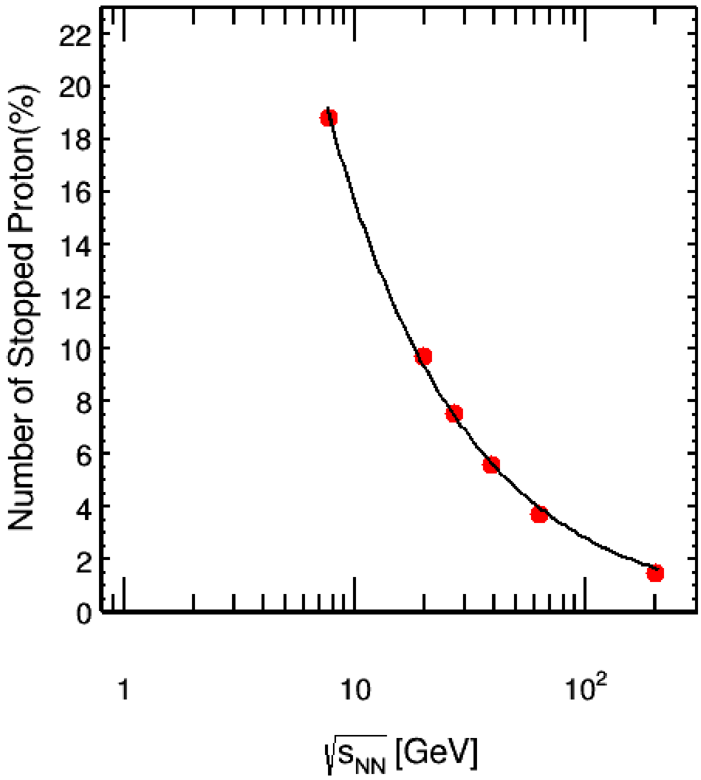

Figure 4.4: The net-proton as a function of $\sqrt{s_{\mathrm{NN}}}$.

approximately 27.27, 20.43, 13.90, 11.03, 8.46, 6.03, 2.60, respectively. Similarly, the protons are also interpolated as shown in Table 4.2 from Fig 4.4. We do an AMPT simulation at the discussed energies to study the invariant yield of protons falling in STAR acceptance. This is discussed in the next section.

4.3 AMPT Simulation

A Multi-Phase Transport model was constructed specifically for the study of relativistic heavy ion collisions. It contains essential stages of heavy ion collisions from the initial condition to final observable on an event-by-event basis, including the parton cascade, hadronization and the hadron cascade. The model can generate events in two different modes: 1. default and 2. string melting (SM). In both modes the initial conditions are taken from HIJING. We use the default mode for simulation in this work. In the default mode, energetic partons cascade through Zhang's Parton Cascade (ZPC) before the strings and partons are recombined and the strings are fragmented via the Lund string fragmentation function,

$$f(z) = z^{-1}(1-z)^a exp(-b{m_T}^2/z), \tag{4.7}$$

where a and b are the Lund string fragmentation function parameters, taken to be 0.2 and 2.2. ART (A Relativistic Transport model for hadrons) is originally developed for heavy ion collisions at the alternating gradient synchrotron (AGS) energies. The default mode describes the evolution of collision in terms of string and mini jets followed by string fragmentation.

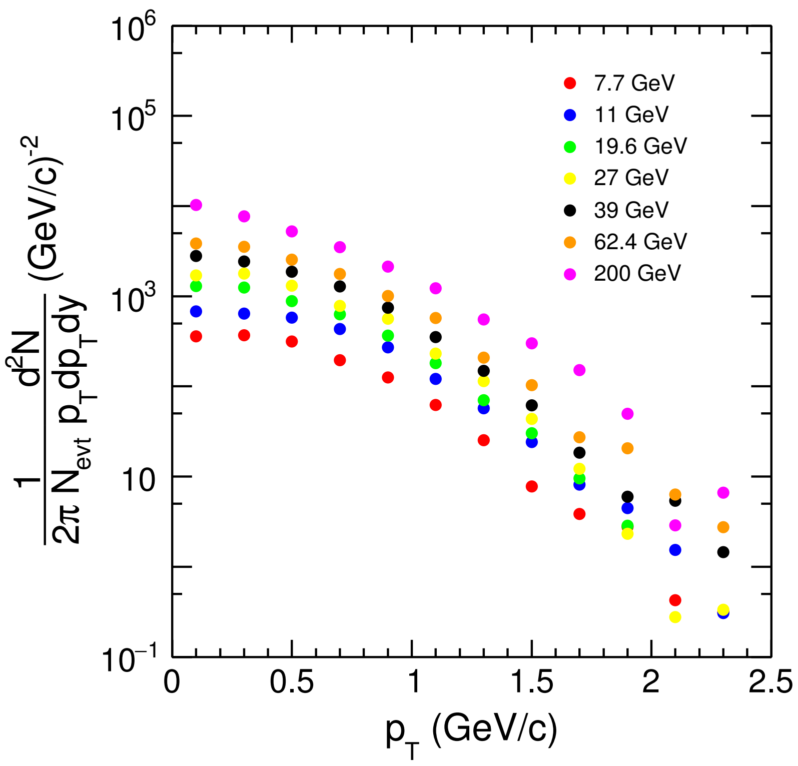

Figure 4.5: Invariant yield of protons using AMPT model at different $\sqrt{s_{\mathrm{NN}}}$

.

The AMPT model has been applied to study many observables at RHIC. We have used AMPT model with default settings to simulate the invariant p_T spectra of protons at different centre-of-mass energies at mid-rapidity ($\eta \pm 0.5$), as is shown in Fig. 4.5. Now to estimate the number of protons in STAR p_T-range (0.4 to 0.8 GeV/c), we calculate the fraction of protons in whole p_T-range to the protons in $0.4 < p_T < 0.8$ GeV/c. We use the same fraction to calculate the stopped protons in STAR acceptance.

Table 4.3: Percentage from p_T spectra at different STAR energies:

$\sqrt{s_{\rm NN}}$[GeV]	7.7	11.5	19.6	27	39	62.4	200
% from p_T Spectra	43.63	43.56	44.31	43.65	43.24	39.74	37.5658

4.4 Estimation of Stopped Protons in STAR Acceptance

Following Table 4.4 summaries the results obtained through different processes as is mentioned in the above sections. To summaries, we calculate the number of protons due to the stopping of colliding nuclei. These stopped protons are estimated at mid-rapidity ($|\eta| < 0.5$). Further, these protons are distributed over whole p_T spectra. To quantify these protons in the STAR momentum range, we have used the AMPT simulation. From AMPT, we calculate the fraction of protons lying in the range of STAR momentum acceptance i.e. ($0.4 \leqslant p_T \leqslant 0.8$ GeV/c). Afterwords, these protons are compared with the STAR protons distribution.

It is interesting to see, the stopped protons measured are less than the STAR proton data, which have contribution from stopping as well as from production. After subtracting i.e. protons without stopping, we compare results with STAR $< \bar{p} >$. The calculations are in good agreement with STAR $< \bar{p} >$ for all available center-of-mass energies from 7.7 to 200 GeV. The importance of this work and future outlooks are described in the next Chapter.

Table 4.4: Summary of protons at different center-of-mass energies:

(a)	(b)	(c)	(d)	(e)	(f)	(g)
$\sqrt{s_{\mathrm{NN}}}$ (GeV)	Total stopped protons in (%)	% of stopped protons in STAR p_T-range	No. of stopped protons in STAR acceptance	STAR protons Data	Protons data w/o stopping	STAR $< \bar{p} >$
7.7	27.27	43.63	18.79	18.92	0.13	0.165
11.5	20.43	43.56	14.02	15.00	0.99	0.49
19.6	13.90	44.32	9.73	11.37	1.64	1.15
27.0	11.03	43.65	7.61	9.39	1.78	1.65
39.0	8.46	43.24	5.78	8.22	2.44	2.38
62.4	6.03	39.74	3.78	7.25	3.47	3.14
200	2.60	37.57	1.54	5.66	4.11	4.11

Chapter 5

Conclusions and Scope for Future Work

The baryon stopping plays an important role in studying the QCD phase diagram and possibly locating the critical end point and/ the equation of state; as this is directly related to the collision energy. The non-monotonic behavior of higher moments of net-proton has been a focus point in recent days. In this work we have tried to subtract out the stopped protons from the net-proton distribution, as the former plays an important role at lower center-of-mass energies.

In the present thesis work, the contribution of protons coming from the colliding nuclei is estimated. Also special emphasis is given to their contribution on the recent net-proton measurements by STAR collaboration. In most of the experiments it is difficult to identify the contribution of resonance decay, produced protons and stopped protons. We have developed a method to estimate and remove the stopped protons from the experimentally measured net-proton fluctuation.

There are many speculations about the non-monotonic behavior at STAR energies [Phys. Rev. Lett. 112, 032302]. It is believed that the decreasing trend at 19.6 GeV may be an indication for QCD-critical end point of phase diagram.

We propose to check this behavior after removing the beam-stopped protons as they play a significant role at lower center-of-mass energies. It will be exciting to see whether the non-monotonic behavior persists after taking out the contribution coming from the stopped protons in the net-proton higher moments. We reserve the further discussion about net-proton fluctuation after correcting STAR measurements for our future works, which is planned to appear in a regular journal publication.

Bibliography

[1] G. Dissertori, I. Knowles, and M. Schmelling, Quantum Chromodynamics - High Energy Experiments and Theory, Oxford University Press (2003).

[2] D. J. Gross and F. Wilczek, Phys. Rev. Lett. **30**, 1343 (1973).

[3] H. D. Politzer, Phys. Rev. Lett. **30**, 1346 (1973).

[4] S. Bethke, Nucl. Phys. Proc. Suppl. **39BC**, 198 (1995).

[5] S. Bethke, Prog. Part. Nucl. Phys. **58**, 351 (2007) [hep-ex/0606035].

[6] C. P. Singh, Phys. Rept. **236**, 147 (1993).

[7] H. Satz, Nucl. Phys. A **418**, 447C (1984).

[8] Z. Fodor and S. D. Katz, Phys. Lett. B **534**, 87 (2002); JHEP **0203**, 014 (2002).

[9] Z. Fodor and S. D. Katz, JHEP **0404**, 050 (2004).

[10] J. Gregg, Archive for History of Exact Sciences **53**, 51 (1998).

[11] E. M. Lifshitz and L. P. Pitaevskii, Course of Theoritical Physics (Third Revised and Enlarged Edition), Volume 5, Pergamon Press, 1980.

[12] K. Fukushima and T. Hatsuda, Rept. Prog. Phys. **74**, 014001 (2011) [arXiv:1005.4814 [hep-ph]].

[13] The Frontiers of Nuclear Science, 2007 NSAC Long Range Plan.

[14] Y. Aoki, G. Endrodi, Z. Fodor, S. D. Katz and K. K. Szabo, Nature **443**, 675 (2006) [hep-lat/0611014].

[15] C. DeTar and U. M. Heller, Eur. Phys. J. A **41**, 405 (2009) [arXiv:0905.2949 [hep-lat]].

[16] K. Nagata and A. Nakamura, EPJ Web Conf. **20**, 03006 (2012) [arXiv:1109.0475 [hep-lat]].

[17] S. K. Tiwari and C. P. Singh, Adv. High Energy Phys. **2013**, 805413 (2013) doi:10.1155/2013/805413 [arXiv:1306.3291 [hep-ph]].

[18] M. A. Stephanov, PoS LAT **2006**, 024 (2006) [hep-lat/0701002].

[19] S. Ejiri, C. R. Allton, S. J. Hands, O. Kaczmarek, F. Karsch, E. Laermann and C. Schmidt, Prog. Theor. Phys. Suppl. **153**, 118 (2004) [hep-lat/0312006].

[20] G. H. Corral, CERN Yellow Report CERN-2010-001, 393-416 [arXiv:1010.3164 [nucl-th]].

[21] M. Gazdzicki and St. Mrowczynski, Z. Phys. C **54** (1992) 127.

[22] J. L. Klay *et al.* [E-0895 Collaboration], Phys. Rev. C **68**, 054905 (2003).

[23] F. Videbaek, J. Phys. Conf. Ser. **50**, 134 (2006)

[24] Y. B. Ivanov, Phys. Lett. B **690**, 358 (2010) [arXiv:1001.0670 [nucl-th]].

[25] I. C. Arsene *et al.* [BRAHMS Collaboration], Phys. Lett. B **677**, 267 (2009) [arXiv:0901.0872 [nucl-ex]].

[26] I. G. Bearden *et al.* [BRAHMS Collaboration], Phys. Rev. Lett. **93**, 102301 (2004)

[27] L. Ahle *et al.* [E802 Collaboration], Phys. Rev. C **60**, 064901 (1999). doi:10.1103/PhysRevC.60.064901

[28] J. Barrette *et al.* [E877 Collaboration], Phys. Rev. C **62**, 024901 (2000)

[29] B. B. Back *et al.* [E917 Collaboration], Phys. Rev. Lett. **86**, 1970 (2001)

[30] Y. B. Ivanov, Phys. Atom. Nucl. **75**, 621 (2012) doi:10.1134/S1063778812050110

[31] J. Stachel, Nucl. Phys. A **654**, no. 1-2, C119 (1999) doi:10.1016/S0375-9474(99)00250-X [nucl-ex/9903007].

[32] H. Appelshauser *et al.* [NA49 Collaboration], Phys. Rev. Lett. **82**, 2471 (1999) doi:10.1103/PhysRevLett.82.2471 [nucl-ex/9810014].

[33] T. Anticic *et al.* [NA49 Collaboration], Phys. Rev. C **69**, 024902 (2004). doi:10.1103/PhysRevC.69.024902

[34] C. Alt *et al.* [NA49 Collaboration], Phys. Rev. C **73**, 044910 (2006). doi:10.1103/PhysRevC.73.044910

[35] C. Blume [Na49 Collaboration], J. Phys. G **34**, S951 (2007) doi:10.1088/0954-3899/34/8/S133 [nucl-ex/0701042].

[36] H. Strobele [NA49 Collaboration], PoS CPOD **2009**, 044 (2009) [arXiv:0908.2777 [nucl-ex]].

[37] E. Schnedermann, J. Sollfrank and U. W. Heinz, Phys. Rev. C **48**, 2462 (1993) doi:10.1103/PhysRevC.48.2462 [nucl-th/9307020].

[38] C. Alt et al, [NA49 Collaboration], Phys. Rev. C **78** (2008) 034914.

[39] G. L. Melkumov et al., [NA49 Collaboration], Nucl. Phys. B. **219-220** (2011), T. Anticic et al., [NA49 Collaboration], Phys. Rev. C **79** (2009) 044904.

[40] T. Anticic et al., [NA49 Collaboration], Phys. Rev. C **83** (2011) 061902.

[41] B. I. Abelev et al., [STAR Collaboration], Phys. Rev. Lett. **103** (2009) 092301.

[42] A. Laszlo *et al.* [NA61 Collaboration], PoS CPOD **07**, 054 (2007) [arXiv:0709.1867 [nucl-ex]].

[43] T. Anticic et al., [NA49 Collaboration], Phys. Rev. C **83** (2011) 061902.

[44] I. Arsene *et al.* [BRAHMS Collaboration], Nucl. Phys. A **757**, 1 (2005) doi:10.1016/j.nuclphysa.2005.02.130 [nucl-ex/0410020].

[45] M. A. Stephanov, K. Rajagopal and E. V. Shuryak, Phys. Rev. Lett. **81**, 4816 (1998).

[46] M. A. Stephanov, Prog. Theor. Phys. Suppl. **153**, 139 (2004), Int. J. Mod. Phys. A **20**, 4387 (2005).

[47] Z. Fodor and S. D. Katz, JHEP **0404**, 050 (2004).

[48] M. A. Stephanov, K. Rajagopal and E. V. Shuryak, Phys. Rev. D **60**, 114028 (1999).

[49] S. Ejiri, F. Karsch and K. Redlich, Phys. Lett. B **633**, 275 (2006).

[50] A. Bazavov, H. T. Ding, P. Hegde, O. Kaczmarek, F. Karsch, E. Laermann, S. Mukherjee and P. Petreczky *et al.*, Phys. Rev. Lett. **109**, 192302 (2012).

[51] M. A. Stephanov, Phys. Rev. Lett. **102**, 032301 (2009).

[52] R. V. Gavai and S. Gupta, Phys. Lett. B **696**, 459 (2011).

[53] M. Cheng, P. Hegde, C. Jung, F. Karsch, O. Kaczmarek, E. Laermann, R. D. Mawhinney and C. Miao *et al.*, Phys. Rev. D **79**, 074505 (2009).

[54] S. Borsanyi, Z. Fodor, S. D. Katz, S. Krieg, C. Ratti and K. K. Szabo, Phys. Rev. Lett. **113**, 052301 (2014).

[55] P. Alba, W. Alberico, R. Bellwied, M. Bluhm, V. Mantovani Sarti, M. Nahrgang and C. Ratti, Phys. Lett. B **738**, 305 (2014).

[56] A. Adare *et al.* [PHENIX Collaboration], Phys. Rev. C **93**, 011901 (2016).

[57] L. Adamczyk *et al.* [STAR Collaboration], Phys. Rev. Lett. **113**, 092301 (2014).

[58] L. Adamczyk *et al.* [STAR Collaboration], Phys. Rev. Lett. **112**, 032302 (2014).

[59] P. Braun-Munzinger, B. Friman, F. Karsch, K. Redlich and V. Skokov, Nucl. Phys. A **880**, 48 (2012).

[60] N. L. Johnson, S. Kotz, and N. Balakrishnan. 1997. Discrete multivariate distributions. New York, NY.: John Wiley & Sons, Inc.

[61] O. E. Barndorff-Nielsen, D. G. Pollard, and N. Shephard, Integer-valued Levy processes and low latency financial econometrics, Quant. Finance 12, 587 (2012).

[62] T. J. Tarnowsky and G. D. Westfall, Phys. Lett. B **724**, 51 (2013).

[63] G. D. Westfall, Phys. Rev. C **92**, 024902 (2015).

[64] P. K. Netrakanti, X. F. Luo, D. K. Mishra, B. Mohanty, A. Mohanty and N. Xu, Nucl. Phys. A **947**, 248 (2016).

[65] X. Luo, B. Mohanty and N. Xu, Nucl. Phys. A **931**, 808 (2014).

[66] R. V. Gavai and S. Gupta, Phys. Lett. B **696** (2011) 459.

[67] F. Karsch and K. Redlich, Phys. Lett. B **695** (2011) 136.

[68] M. Asakawa, S. Ejiri and M. Kitazawa, Phys. Rev. Lett. **103** (2009) 262301.

[69] P. Braun-Munzinger, K. Redlich and J. Stachel, In *Hwa, R.C. (ed.) et al.: Quark gluon plasma* 491-599 [nucl-th/0304013].

[70] D. McDonald [STAR Collaboration], arXiv:1210.7023 [nucl-ex].

[71] J. T. Mitchell [PHENIX Collaboration], arXiv:1211.6139 [nucl-ex].

[72] V. P. Konchaovski, M. I. Gorenstein, E. L. Bratkovskaya and H. Stocker, Phys. Rev. C **74** (2006) 064911.